Experimental Investigation of Coannular Jet Flow with Swirl Along a Centerbody

M. O. Frey* and F. B. Gessner†
University of Washington, Seattle, Washington 98195

An experimental study was conducted in order to investigate the nature of incompressible coannular jet flow with swirl along an unconfined centerbody. Swirl was imparted to the inner stream upstream of the nozzle exit, and the ratio of the outer-to-inner stream mass flow rate ratio was fixed at unity. The results indicate that the flow is dominated by coherent structures in the form of vortices that are shed periodically from the lips of the nozzle. The presence of these vortices leads to large departures from local equilibrium, as indicated by the sign of the turbulent shear stress, which does not always follow the sign of the local mean rate of strain. This behavior causes the axial eddy viscosity component to vary widely throughout the flow and be negative in the inner region of the mixing layer. Vortex-induced turbulence amplification also elevates turbulence kinetic energy levels in regions of the flow where turbulence kinetic energy production rates have diminished. Analysis of the data shows that closure at the full Reynolds stress transport equation level is required if the main features of the flow are to be predicted with reasonable accuracy.

Nomenclature

$c_{\phi 1}$, $c_{\phi 2}$	= empirical coefficients, Eqs. (9–12)
D	= centerbody diameter, Fig. 3
D_i	= nozzle lip diameter, Fig. 3
k	= turbulence kinetic energy
M	= radial gradient of tangential angular momentum, Eq. (15)
$\dot{m}_i$	= mass flow rate of inner stream
$\dot{m}_o$	= mass flow rate of outer stream
P	= static pressure or turbulence kinetic energy production rate
P_∞	= ambient static pressure
R	= centerbody radius, Fig. 3
Re'	= unit Reynolds number, $U_{b,i}/\nu$
R_i, R_o	= nozzle lip radii, Fig. 3
Ri_f	= flux Richardson number, Eq. (13)
Ri_g	= gradient Richardson number, Eq. (14)
S	= swirl number, Eq. (1)
u, v, w	= velocity fluctuations in the x, r, and θ directions, respectively
U, V, W	= mean velocity components in the x, r, and θ directions, respectively
$U_{b,i}$	= bulk velocity of inner stream at $x = 0$
U_i	= core velocity of inner stream at nozzle exit
U_0	= core velocity of outer stream at nozzle exit
U_s	= streamwise mean velocity (vector sum of U and W)
u_s'	= rms velocity fluctuation in the direction of U_s
$\overline{u^2}$, $\overline{v^2}$, $\overline{w^2}$	= Reynolds normal stress components
$\overline{uv}$, $\overline{uw}$, $\overline{vw}$	= Reynolds shear stress components
x, r, θ	= cylindrical coordinates, Fig. 3
α, β, γ	= empirical coefficients, Eqs. (7) and (8)
β	= swirl angle, $\tan^{-1}(W/U)$
ϵ	= turbulence kinetic energy dissipation rate
ν	= kinematic viscosity
ν_{xr}, $\nu_{r\theta}$	= eddy viscosity components, Eqs. (4) and (5)
ν_{xr}', $\nu_{r\theta}'$	= eddy viscosity components, Eqs. (9) and (10)
ν_{xr}'', $\nu_{r\theta}''$	= eddy viscosity components, Eqs. (11) and (12)

Presented as Paper 90-1622 at the AIAA 21st Fluid Dynamics, Plasmadynamics, and Lasers Conference, Seattle, WA, June 18-20, 1990; received July 9, 1990; revision received Oct. 15, 1990; accepted for publication Oct. 15, 1990.

*Research Assistant, Department of Aeronautics and Astronautics.
†Professor, Department of Mechanical Engineering. Member AIAA.

Introduction

PREVIOUS studies of unconfined coaxial jet flows, both with and without swirl, have focused on local flow development downstream of the nozzle exit in the absence of a centerbody.[1-4] In the present study, the mixing of two coannular streams in the presence of a centerbody is considered in order to examine a flow that simulates the essential features of a swirling turbofan engine flow mixing with an axially directed bypass flow. The overall flow situation can be represented schematically, as shown in Fig. 1. Flow emanating from the coannular nozzle consists of two shear layers that interact with each other and with the turbulent boundary layer on the centerbody surface. The flow is complicated by the presence of coherent structures in the flow in the form of embedded vortices, which are shed periodically from the lips of the nozzle. These vortices have been observed in a turbulent jet by Lau and Fisher[5] and Bruun,[6] who applied time-domain averaging techniques to detect their presence. Vortex trains within the inner and outer shear layers of a coaxial jet have also been observed by Ko and his co-workers,[7-9] who employed correlation and conditional sampling techniques to investigate their influence on the local flow structure. Results presented by Kwan and Ko[8] show, for example, that when the core flow velocity of the outer stream is less than that of the inner stream (an operating condition simulated in the present study), then

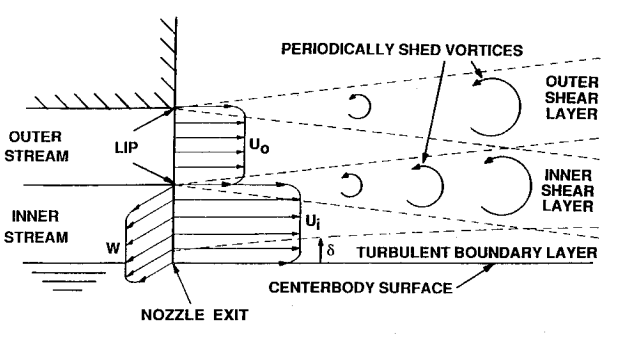

Fig. 1 Local flow behavior in the vicinity of the nozzle exit and centerbody surface.

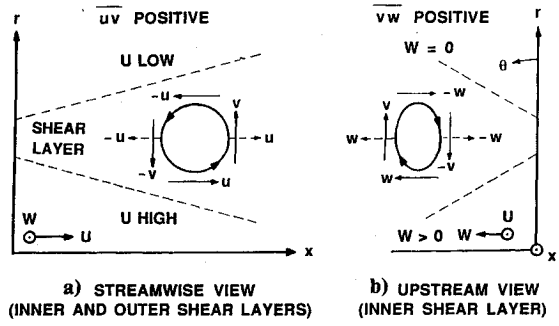

Fig. 2 Proposed mechanism for turbulent shear stress generation from periodic vortical motion.

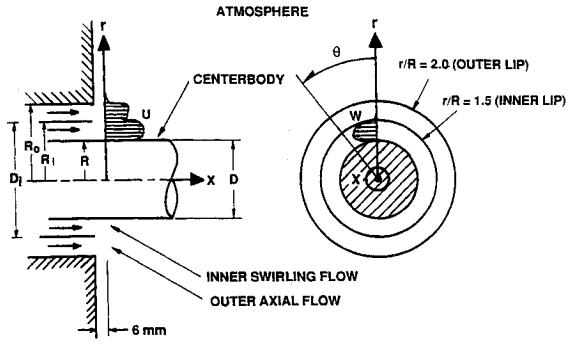

Fig. 3 Flow configuration and coordinate system.

the passage frequency of vortices in the outer shear layer (relative to a fixed observer) is less than that of vortices within the inner shear layer. This behavior is compatible with the vortex patterns shown in Fig. 1.

The process by which a vortex train can lead to increased Reynolds stress levels within a mixing layer has been discussed by Lau and his coworkers.[5,10] In one of their studies,[10] an "extended vortex model" is proposed that describes how the periodic passage of vortices in a mixing layer bounded by an inner potential core ($U>0$) and outer ambient surroundings ($U=0$) can increase Reynolds shear stress levels in that layer. The authors' arguments can be extended to the present flow situation by recognizing that each shear layer in Fig. 1 is initially bounded by regions of relatively high and low axial mean velocity, as indicated in Fig. 2a. Under these conditions, a positive $\overline{uv}$ shear stress will exist within each layer on the basis of mean shear considerations alone, inasmuch as $\partial U/\partial r$ is negative throughout both layers. The magnitude of the shear stress may be augmented, however, by the motion of vortices on the basis of the following considerations: As the leading edge of a vortex is convected past a stationary observation point, the vortical motion will induce a radial outflow of relatively high velocity fluid from the inner region bounding the shear layer. Conversely, relatively low velocity fluid from the outer region will be transported radially inward as the trailing edge of the vortex passes the observation point. This sequence of events gives rise to an induced positive u fluctuation when v is positive (leading edge condition) and an induced negative u fluctuation when v is negative (trailing edge condition). This behavior is shown schematically in Fig. 2a, where the solid arrows depict fluctuations associated with vortex translation past a stationary point, and the dashed arrows depict fluctuations induced by the convecting action of the vortex. In a time-averaged sense, therefore, vortex motion will induce a positive contribution to the $\overline{uv}$ stress component to complement the level induced by mean shear effects alone.

If swirl is present in the flow, as shown in Fig. 1, then flow in the inner shear layer is skewed relative to the xr plane. The projection of a shed vortex in that layer onto the $r\theta$ plane would then appear as shown in Fig. 2b, noting that this layer is bounded by an inner region where W is positive and an outer region where $W=0$. Under these conditions, the v and w fluctuation pattern is as shown in the figure, so that vortex-induced fluctuations will make a positive contribution to $\overline{vw}$ in a time-averaged sense. Inasmuch as $r\partial(W/r)\partial r$ is negative within the inner shear layer for the conditions shown in Fig. 1, the mean shear will also make a positive contribution to $\overline{vw}$, so that both effects again complement each other. The overall process is, of course, complicated by such events as vortex pairing and shear layer merging, but both mechanisms for Reynolds shear stress generation will still exist in merged regions downstream of the initial mixing region, as long as vortices are present within the shear layer.

In addition to vortex-induced effects in the flow, one must also consider the possible influences of centrifugal-related instabilities, noting that negative gradients of angular momentum exist in the inner shear layer for the operating conditions shown in Fig. 1. These instabilities do not have a significant effect on the flow, however, because shear-layer induced instabilities (periodically shed vortices) dominate the present flow situation, as demonstrated by Frey and Gessner[11] in a related paper. In that paper, profiles of the three mean velocity components and six Reynolds stress components are presented at various streamwise locations downstream of the nozzle exit. These results show how the flow develops in the initial mixing region and in the merged region downstream for the operating conditions shown in Fig. 1 ($U_i > U_o$ with swirl present in the inner stream). The paper by Frey and Gessner also includes a discussion of local flow behavior in the vicinity of the centerbody from the point of view of specifying wall functions in this region for prediction purposes. In the present paper, the effects of vortex shedding are analyzed with respect to their influence on the development of the two shear layers that emanate from the coannular nozzle as they interact with each other and with the centerbody boundary layer. This is done by examining turbulence kinetic energy production rates, eddy viscosity component behavior, Richardson number behavior, and phase differences between stress/mean strain rate angles in the flow.

Experimental Program

The overall flow facility is the same as the one described by Mattingly and Oates,[12] except that their blow-down air supply was replaced by a continuously operating high-pressure fan. Flow from the fan was split into two streams, which then passed through a dual concentric plenum chamber fitted with honeycombs and streams. Swirl was imparted to the inner stream by means of 20 equally spaced stator blades in the plenum chamber having an NACA 0024 cross section. The swirl generator was designed to provide a nominally constant swirl angle of approximately 35 deg, corresponding to a swirl number of 0.52 at the nozzle exit. The swirl number was evaluated from an expression that represents the ratio of the axial flux of swirl momentum to axial momentum for the inner stream, namely,

$$S = \int_R^{R_i} (\rho UW + \rho\,\overline{uw})r^2\,dr \Big/ R\int_R^{R_i} [\rho U^2 + \rho\overline{u^2} + (P - P_\infty)]r\,dr \tag{1}$$

The inner stream was bounded by a polished aluminum centerbody, 101.6 mm in diameter, that extended both upstream and downstream of the nozzle exit, as shown in Fig. 3. The inner and outer streams were separated by a thin aluminum tube having an inside diameter of 152.4 mm and a lip thickness of 1.2 mm at the nozzle exit. The outer stream was bounded by a converging section with an exit diameter of 199 mm. For these dimensions, the inner and outer lips of the nozzle were located at $r/R = 1.5$ and 2.0, respectively, as shown in Fig. 3. The two streams exited from the nozzle at room temperature (17 C), and the two flow rates were adjusted to yield an

outer-to-inner mass flow rate ratio of unity ($\dot{m}_o/\dot{m}_i = 1$). For all of the results reported in this paper, the axial bulk velocity of the inner stream, $U_{b,i}$, was 11.7 mps at the first station where data were taken ($x/D = 0$, which is 6 mm downstream of the nozzle exit, as shown in Fig. 3). The corresponding unit Reynolds number Re' was 7.8×10^5 m^{-1}.

Pressure probe data were taken using a 1.5 mm (0.062 in.) OD pitot-static tube, a 0.7 mm (0.028 in.) OD total pressure probe, and a 0.6 mm (0.024 in.) OD Conrad (yaw angle) probe with an apex angle of 75 deg. The static pressure on the centerbody surface was measured by means of 0.5 mm (0.020 in.) diameter wall taps connected to a Type J, 48-port Scanivalve. Differential pressures were read on a Datametrics Type 1400 electronic manometer connected to a Datametrics Type 590D-10W-2P8-V1X-4D Barocel pressure transducer. Initial data were taken at six axial stations ($x/D = 0$, 0.5, 1.5, 3.0, 4.5, and 6.0) with the Conrad probe by operating it in the nulling mode in order to determine the radial variation of the swirl (yaw) angle β, defined as $\tan^{-1}(W/U)$. Subsequent data were taken with the pitot-static and total pressure probes nominally aligned in the yaw plane at each measuring point in order to evaluate the local static pressure and the magnitude of the resultant mean velocity component in this plane. This procedure presumes that the radial velocity component V is small in comparison to U and W, a condition later verified by the hot-wire measurements. Pressure probe data taken near the nozzle exit (at $x/D = 0$) indicated that the skewed boundary layer on the centerbody surface was fully turbulent and in agreement with the law-of-the-wall at this location.

Hot-wire data were taken at the six axial stations by means of forward facing probes nominally aligned with the mean flow direction in the yaw plane, as determined from the Conrad probe measurements. The sensing element of each probe was 4μ (0.00015 in.) diam platinum-plated tungsten wire with a centered active length of 1 mm (0.040 in.) between probe fingers approximately 4 mm (0.16 in.) apart. The hot-wire measurements were made by applying the single-wire probe rotation technique developed by Al-Beirutty and Gessner.[13] This technique is based on the sequential use of normal and slant-wire probes, and is second-order accurate relative to the fluctuations, a feature that enhances measurement accuracy in moderate intensity flows. The hot-wire probes were energized by a TSI Model 1010 constant temperature anemometer connected to a DISA Type 55M25 linearizer. The mean linearized output voltage was read on a DISA Type 55D31 digital voltmeter. The mean square of the fluctuating linearized output voltage was read on a second DISA Type 55D31 digital voltmeter connected to a TSI Model 1060 rms voltmeter. Hot-wire calibration, measurement, and data reduction procedures for the present series of experiments are described in more detail by Frey and Gessner.[11] That reference also includes details of the probe configurations and uncertainty estimates for the basic variables, as calculated from the linearized uncertainty model described by Al-Beirutty.[14] All of the experimental results discussed in the next section are based on hot-wire measurements, with the exception of the swirl angle, which is based on data obtained with the Conrad probe.

Results and Discussion

Basic Flow Behavior

The variation of swirl angle ($\beta \equiv \tan^{-1} W/U$) with axial position over the interval $0 \le x/D \le 6.0$ is shown in Fig. 4a for the inner mixing region ($0 \le r/R \le 1.5$). This figure shows that the local flow angle decreases continuously along traverses parallel to the centerbody at and near $r/R = 1.5$, with no evidence of vortex-induced periodicity in the flow. In the relatively low momentum fluid adjacent to the centerbody surface, however, distinct oscillations appear that are especially evident along the first traverse ($r/R = 1.003$). The period of the initial oscillation on this traverse ($1.27D_i$) is comparable to vortex shedding periods observed in a turbulent jet[5] ($1.25D_i$) and in the inner mixing region of coaxial jets ($1.20D_i$) for similar operating conditions. In the downstream region ($x/D \ge 4.0$), Fig. 4b shows that these oscillations no longer appear in the immediate vicinity of the centerbody surface, which implies that the coherent vortex structure has diminished in strength or even disappeared as a result of vortex breakup in the centerbody boundary layer.

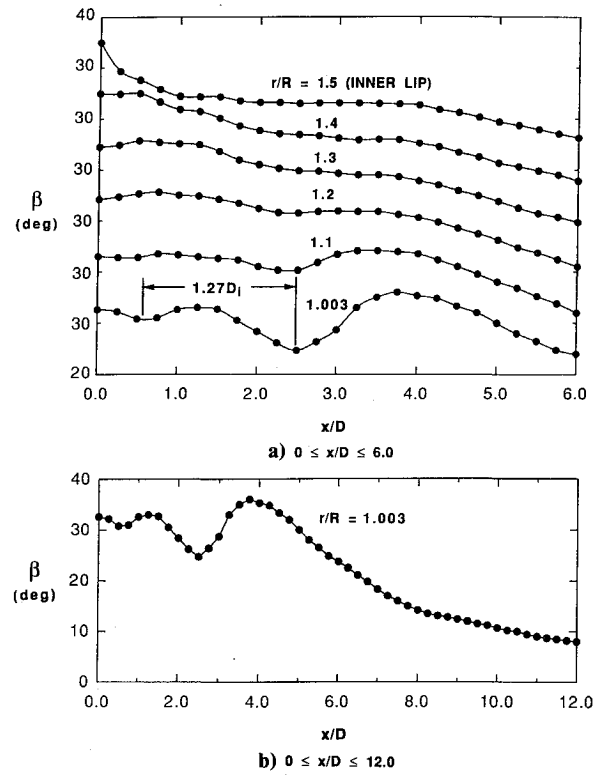

Fig. 4 Swirl angle variation in the inner region of the mixing layer.

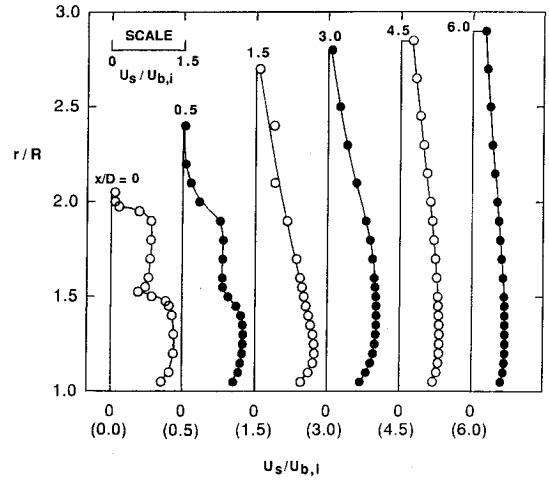

Fig. 5 Streamwise mean velocity profiles.

The behavior of the streamwise mean velocity U_s (defined as the vector sum of U and W) as the flow develops between $x/D = 0$ and 6.0 is shown in Fig. 5. Corresponding velocity component (U and W) profiles are presented in the related paper by Frey and Gessner.[11] In reference to the profiles shown in Fig. 5, it is difficult to see any outward manifestations of vortex-induced effects. The inner and outer streams merge, decay, and spread in accordance with anticipated behavior, with no anomalies present in the distributions. This is not the case for the local streamwise intensity, however, where, in reference to Fig. 6, it can be seen that turbulence levels near the centerbody surface increase, rather than decay, in the downstream direction. This behavior is not directly attributable to the spreading shear layer, because peak inten-

sity levels in the inner layer near the nozzle lip (at $r/R = 1.5$) are less than downstream levels near the centerbody surface. Instead, a more likely source for elevated intensity levels near the centerbody surface is vortex breakup into chaotic motion as the inner shear layer interacts with the centerbody boundary layer. This point of view is compatible with the changes that occur in the flow angle distributions shown in Fig. 4b.

Reynolds shear stress profiles measured at the six axial stations are presented in Fig. 7. In this figure, $\overline{uv}$ and $\overline{vw}$ profiles (the solid-line distributions) are shown relative to mean strain rates acting in the same plane, $\partial U/\partial r$ and $r\partial(W/r)/\partial r$, respectively (the dashed-line distributions). In reference to the outer region of the flow, $\overline{uv}$ and $\overline{vw}$ are opposite in sign to $\partial U/\partial r$ and $r\partial(W/r)/\partial r$, respectively, at all six stations, which is in accord with anticipated behavior. At $x/D = 4.5$ and 6.0, shear stress levels are relatively high in comparison to mean strain rates, however, which implies that shear stress levels in the outer region are sustained primarily through vortex-induced effects, rather than directly by mean strain rates in the flow. This reasoning is based on the extended vortex model described earlier, which provides a mechanism for augmenting both $\overline{uv}$ and $\overline{vw}$ stress levels in the flow when swirl is present (refer to Fig. 2). In reference to the results show in Fig. 7a, it can be seen that the change in sign of $\overline{uv}$ at the first two stations ($x/D = 0$ and 0.5) correlates well with the change in sign of $\partial U/\partial r$ across the width of the shear layer. At $x/D = 3.0$, however, it can be seen that $\overline{uv}$ changes sign in a region where $\partial U/\partial r$ remains positive, which indicates that strong departures from local equilibrium have occurred. This observation is supported by the results shown in Fig. 7b, specifically in the vicinity of the centerbody surface, where $\overline{vw}$ remains near zero in a region where $r\,\partial(W/r)/\partial r$ is strongly positive.

The complexity of the flow can also be illustrated by examining the behavior of stress/mean strain rate angles in the flow. If the resultant turbulent shear stress is aligned with the mean strain rate, then the orientation angle of the resultant shear stress, namely $\tan^{-1}(-\overline{vw}/-\overline{uv})$, should be coincident with the orientation angle of the mean strain rate, i.e., $\tan^{-1}[r\partial(W/r)/\partial r]/(\partial U/\partial r)$. Figure 8 shows the variation of these angles along radial traverses at two axial stations ($x/D = 1.5$ and 3.0). In the outer region of the flow ($r/R \geq 1.8$), shear stress and strain rate angles are close to each other, which implies that the resultant shear stress is nominally aligned with the mean strain rate in this region. Figure 8 shows that the strain rate angle approaches the local flow angle on the centerbody surface at both $x/D = 1.5$ and 3.0. Similar behavior has been observed in other types of three-dimensional skewed boundary-layer flows.[15-16] Figure 8 also indicates that stress angles tend to lag behind strain rate angle in approaching the flow angle on the centerbody surface. This behavior exists in a region where vortex-induced oscillations in the flow are particularly severe (refer to Fig. 4). In the midregion of the flow ($1.2 \leq r/R \leq 1.6$), the phase difference between stress and strain rate angles is approximately 30 deg at $x/D = 1.5$ (Fig. 8a), and increases to more than 90 deg at $x/D = 3.0$ (Fig. 8b). These large variations are the direct result of having $\overline{uv}$ change sign at a radial position where $\overline{vw}$ remains positive, and of having the mean strain rate components $\partial U/\partial r$ and $r\partial(W/r)/\partial r$ change sign at different radial locations (compare Figs. 7a and 7b).

Turbulence kinetic energy profiles measured at the six axial stations are shown in Fig. 9. At the first station ($x/D = 0$), the turbulence kinetic energy profile is in accord with anticipated behavior; i.e., k first decreases with increasing distance from the centerbody surface, peaks near $r/R = 1.5$ where the inner and outer streams exiting from the nozzle initially merge, and then decays to zero in the outer stream where the mean shear is relatively low. As the flow progresses downstream, k increases, both in the vicinity of the centerbody and in the outer mixing region. At $x/D = 6.0$, for example, turbulence kinetic

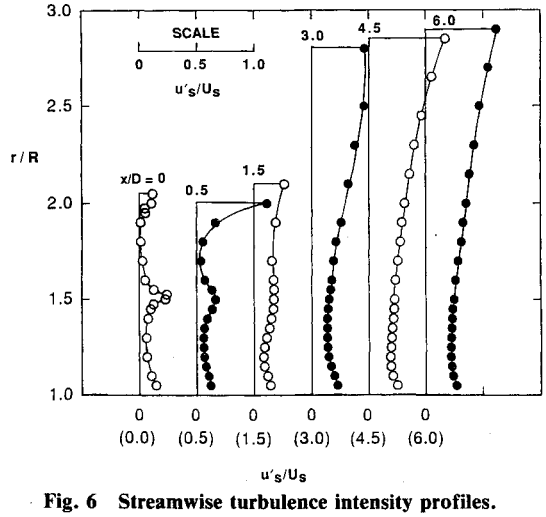

Fig. 6 Streamwise turbulence intensity profiles.

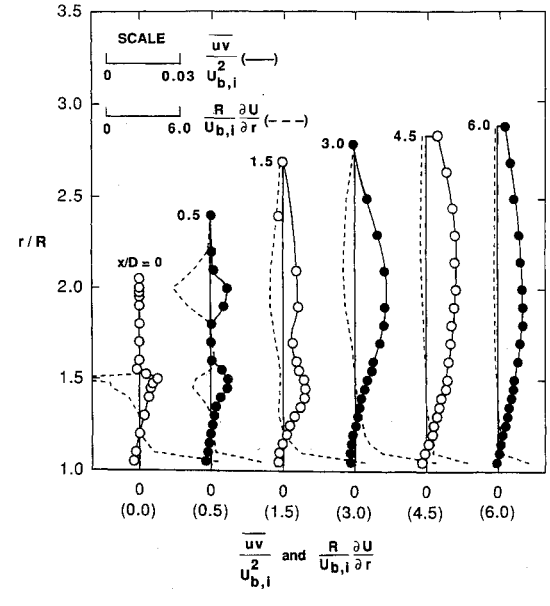

a) COMPONENTS IN xr PLANE

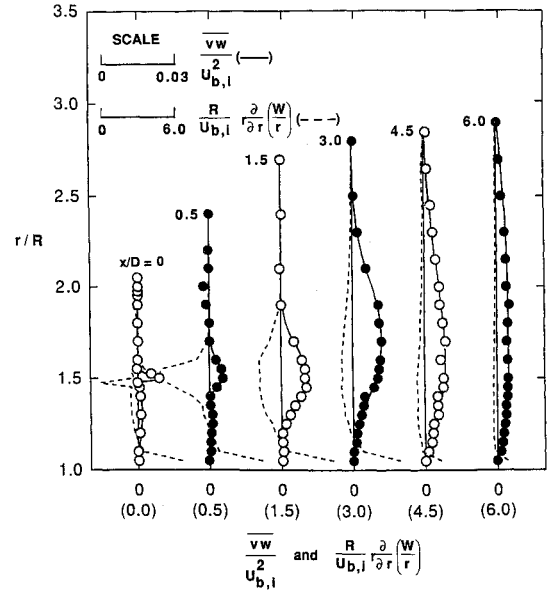

b) COMPONENTS IN rθ PLANE

Fig. 7 Turbulent shear stress and mean strain rate component profiles.

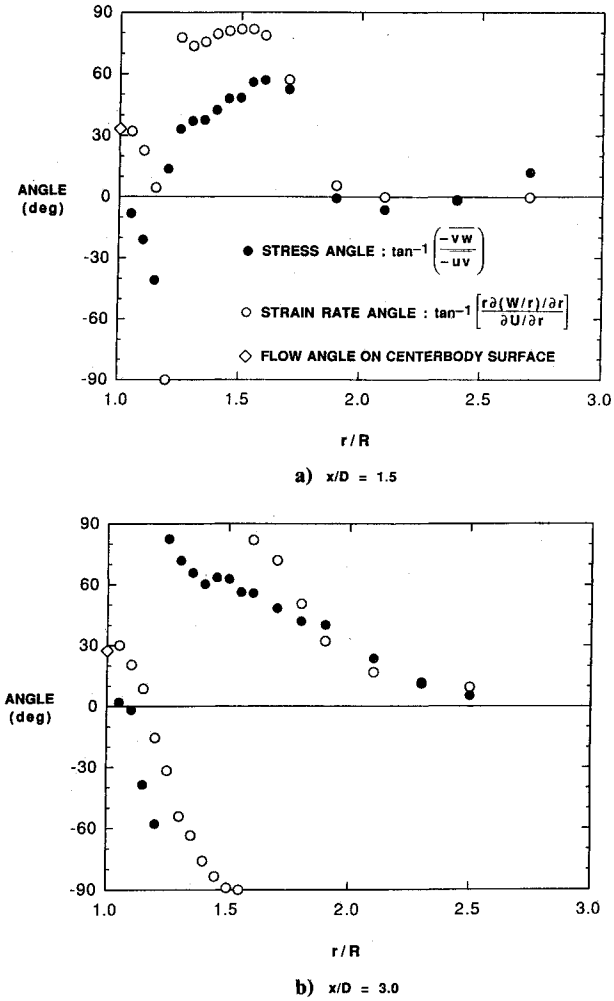

Fig. 8 Resultant turbulent shear stress and mean strain rate angle distributions.

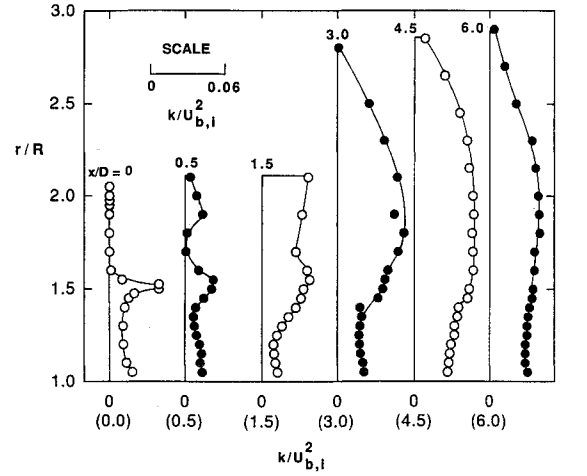

Fig. 9 Turbulence kinetic energy profiles.

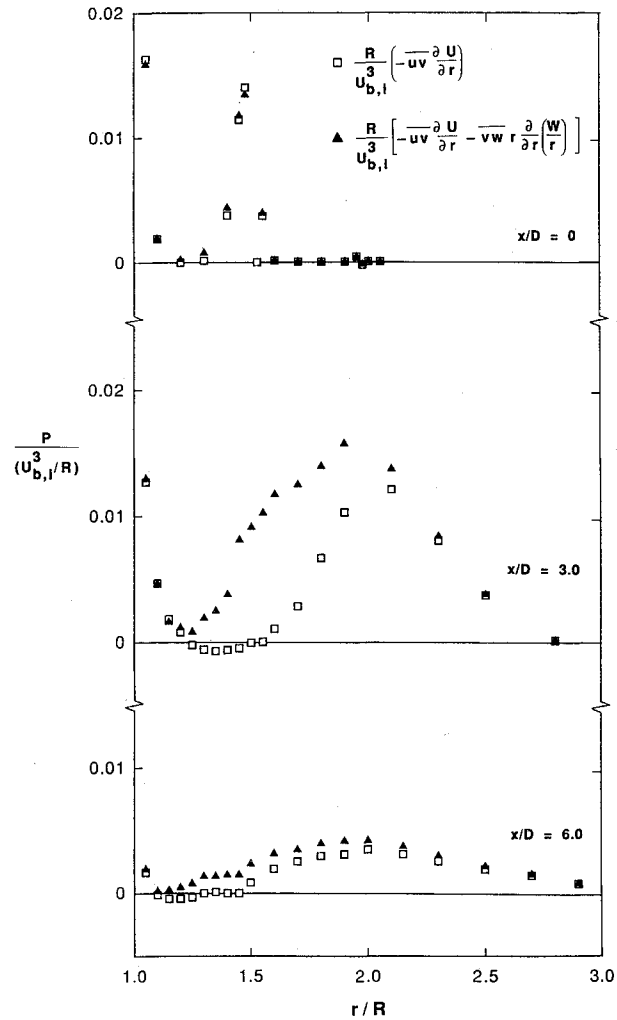

Fig. 10 Turbulence kinetic energy production rate distributions.

energy levels near the centerbody surface are more than twice the levels at $x/D = 0$, even though mean strain rates in this region have diminished (refer to Fig. 7).

Some insight into this behavior can be gleaned by examining turbulence kinetic energy production rates in the flow. In general, the turbulence kinetic energy production rate in cylindrical coordinates for axisymmetric flows can expressed as[17]:

$$P = -\overline{u^2}\frac{\partial U}{\partial x} - \overline{v^2}\frac{\partial V}{\partial r} - \overline{w^2}\frac{V}{r} - \overline{uv}\left(\frac{\partial U}{\partial r} + \frac{\partial V}{\partial x}\right) - \overline{uw}\frac{\partial W}{\partial x} - \overline{vw}\,r\frac{\partial}{\partial r}\left(\frac{W}{r}\right) \tag{2}$$

If the boundary-layer approximations appropriate for the present flow situation are applied, then Eq. (2) reduces to

$$P = -\overline{uv}\frac{\partial U}{\partial r} - \overline{vw}\,r\frac{\partial}{\partial r}\left(\frac{W}{r}\right) \tag{3}$$

Figure 10 shows production rate profiles evaluated from Eq. (3) at three stations ($x/D = 0$, 3.0, and 6.0). At $x/D = 0$, almost all of the turbulence kinetic energy production across the entire shear layer is due to $-\overline{uv}\,\partial U/\partial r$. The changes in production rate that occur across the shear layer at $x/D = 0$ are compatible with the radial variations in k that occur at this location (refer to Fig. 9). At $x/D = 3.0$, Fig. 10 shows that although $-\overline{uv}\,\partial U/\partial r$ continues to be the primary contributor to production in the inner and outer regions, $-\overline{vw}\,r\partial(W/r)/\partial r$ makes a significant contribution to the production rate in the midregion of the shear layer ($1.4 \le r/R \le 2.0$). At $x/D = 6.0$, the results are qualitatively similar to those at $x/D = 3.0$, except that production rates are uniformly much smaller across the entire width of the shear layer. These results are not entirely compatible with the turbulence kinetic energy profiles in Fig. 9. For example. Fig. 9 shows that k increases near the centerbody surface between $x/D = 0$ and 6.0, while Fig. 10 indicates that the turbulence kinetic energy production rate in this region steadily decreases. Figure 9 also shows that k levels within the interval $1.5 \le r/R \le 2.5$ tend to stay relatively constant between $x/D = 3.0$ and 6.0, whereas Fig. 10 clearly

shows that production rates within this interval have diminished significantly.

The apparently low-turbulence kinetic energy production rates are not attributable to using Eq. (3), rather than Eq. (2), to evaluate P, inasmuch as the omitted terms are all at least an order of magnitude smaller than the terms that appear in Eq. (3). The production rates shown in Fig. 10 are quantitatively correct, therefore, and elevated k levels exist in the flow as a result of vortex-induced turbulence amplification, either through coherent vortex motion or after vortex breakup. Both mechanisms would tend to enhance turbulence kinetic energy levels without simultaneously inducing an increase in the mean shear. This conjecture is compatible with the results shown in Figs. 5 and 9, which indicate that high-turbulence kinetic energy levels are sustained in regions where the resultant mean shear has diminished.

The behavior of the $\overline{uv}$ and $\overline{vw}$ profiles shown in Fig. 7 relative to mean strain rates acting in the same plane implies that the eddy viscosity is not a scalar quantity and is not always positive throughout the flow. In order to quantify this behavior, eddy viscosity components were evaluated from the data by means of relationships that apply for swirling turbulent flow after the boundary-layer approximations are applied, namely[16,18]:

$$\nu_{xr} = \frac{-\overline{uv}}{\partial U/\partial r} \tag{4}$$

$$\nu_{r\theta} = \frac{-\overline{vw}}{r\partial(W/r)/\partial r} \tag{5}$$

Distributions of ν_{xr} and $\nu_{r\theta}$ across the width of the shear layer at $x/D = 3.0$, 4.5, and 6.0 are shown in Fig. 11. In reference to Fig. 11a, it can be seen that ν_{xr} is negative in the inner region ($1.0 < r/R < 1.5$), but then becomes positive in the outer region ($r/R \geq 1.5$). This behavior is directly attributable to the change in sign of $\partial U/\partial r$ that occurs near $r/R = 1.5$, while $\overline{uv}$ remains positive in this region (refer to Fig. 7a). By contrast, $\nu_{r\theta}$ remains positive across the width of the shear layer, as shown in Fig. 11b, because $\overline{vw}$ and $r\partial(W/r)/\partial r$ are of the opposite sign at each radial location. This overall behavior cannot be modeled within the context of conventional algebraic Reynolds stress models, as will now be demonstrated.

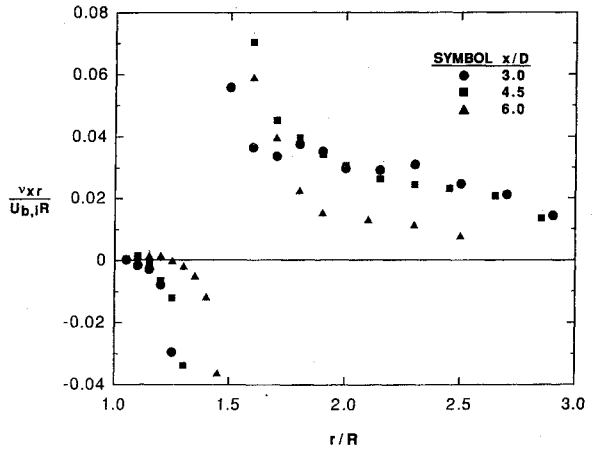

a) COMPONENT IN xr PLANE

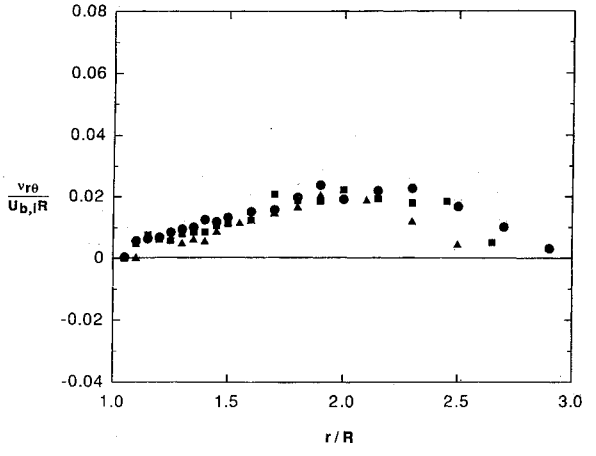

b) COMPONENT IN rθ PLANE

Fig. 11 Eddy viscosity component distributions.

Turbulence Modeling Considerations

In reference to Eqs. (4) and (5), the eddy viscosity ratio $\nu_{xr}/\nu_{r\theta}$ can be written as

$$\frac{\nu_{xr}}{\nu_{r\theta}} = \frac{\overline{uv}/(\partial U/\partial r)}{\overline{vw}/[r\partial(W/r)/\partial r]} \tag{6}$$

which, on the basis of the results shown in Fig. 11, will deviate significantly from unity across the width of the shear layer. This behavior can be compared with that prescribed by relationships derived from the Reynolds stress transport equations after convection and diffusion effects are neglected and the boundary-layer approximations for swirling turbulent flow are applied. If these approximations are applied to the modeled form of the Reynolds stress transport equations proposed by Launder, et al.[19] as referenced by Morse,[17] then reduced forms of the transport equations for $\overline{uv}$ and $\overline{vw}$ can be written respectively as

$$0 = -c_{\phi 1}\frac{\epsilon}{k}\overline{uv} - \left[(1-\alpha)\,\overline{v^2} - \beta\,\overline{u^2} + \frac{\gamma}{2}k\right]\frac{\partial U}{\partial r} \tag{7}$$

$$0 = -c_{\phi 1}\frac{\epsilon}{k}\overline{vw} - \left[(1-\alpha)\,\overline{v^2} - \beta\,\overline{w^2} + \frac{\gamma}{2}k\right]\frac{\partial W}{\partial r} + \left[(1-\alpha)\,\overline{w^2} - \beta\,\overline{v^2} + \frac{\gamma}{2}k\right]\frac{W}{r} \tag{8}$$

where the terms in each equation represent a balance between production and redistribution effects. If Eqs. (7) and (8) are combined with Eqs. (4) and (5), then the eddy viscosity components can be expressed as

$$\nu'_{xr} = \frac{1}{c_{\phi 1}}\frac{k}{\epsilon}\left[(1-\alpha)\,\overline{v^2} - \beta\,\overline{u^2} + \frac{\gamma}{2}k\right] \tag{9}$$

and

$$\nu'_{r\theta} = \frac{1}{c_{\phi 1}}\frac{k}{\epsilon}\left\{\left[(1-\alpha)\,\overline{v^2} - \beta\,\overline{w^2} + \frac{\gamma}{2}k\right]\frac{\partial W/\partial r}{r\partial(W/r)/\partial r} - \left[(1-\alpha)\,\overline{w^2} - \beta\,\overline{v^2} + \frac{\gamma}{2}k\right]\frac{W/r}{r\partial(W/r)/\partial r}\right\} \tag{10}$$

where $\alpha = (8 + c_{\phi 2})/11$, $\beta = (8c_{\phi 2} - 2)/11$, and $\gamma = (60c_{\phi 2} - 4)/55$. Alternate expressions for ν_{xr} and $\nu_{r\theta}$, referred to in the pressure-strain model proposed by Naot et al.[20] can be developed from Eqs. (9) and (10) by letting $\alpha = c_{\phi 2}$ and $\beta = \gamma = 0$, which yields

$$\nu''_{xr} = \frac{(1-c_{\phi 2})}{c_{\phi 1}}\frac{k}{\epsilon}\overline{v^2} \tag{11}$$

$$\nu''_{r\theta} = \frac{(1-c_{\phi 2})}{c_{\phi 1}}\frac{k}{\epsilon}\left[\overline{v^2}\frac{\partial W/\partial r}{r\partial(W/r)/\partial r} - \overline{w^2}\frac{\partial W/\partial r}{r\partial(W/r)/\partial r}\right] \tag{12}$$

In reference to Eqs. (11) and (12), it can be seen that $\nu''_{xr}/\nu''_{r\theta} = 1.0$ when $\overline{v^2} = \overline{w^2}$, a condition that implies that the eddy viscosity should behave as a scalar quantity in regions where $\overline{v^2} \cong \overline{w^2}$. The condition $\overline{v^2} = \overline{w^2}$ applies approximately when $r/R \geq 1.2$ for the present flow (refer to Fig. 12), but as Fig. 11 clearly indicates, ν_{xr} is generally not equal to $\nu_{r\theta}$ in this region. To quantity this behavior, the eddy viscosity ratio $\nu_{xr}/\nu_{r\theta}$ was evaluated from the results shown in Fig. 11. For purposes of comparison, the ratios $\nu'_{xr}/\nu'_{r\theta}$ and $\nu''_{xr}/\nu''_{r\theta}$ were evaluated from Eqs. (9–12), with $c_{\phi 2}$ specified as 0.4 (corresponding to the value suggested by LRR). The results are shown in Fig. 13. From the figure it can be seen that $\nu_{xr}/\nu_{r\theta}$ changes sign near the centerbody surface (from positive to negative), undergoes another change in sign near $r/R = 1.5$, and then remains positive and approaches unity in the outer region of the flow. This behavior is not simulated by either $\nu'_{xr}/\nu'_{r\theta}$ or $\nu''_{xr}/\nu''_{r\theta}$, both of which remain positive and approach unity more quickly than $\nu_{xr}/\nu_{r\theta}$. The situation does not improve when $\overline{uw}$ stress component terms are included in Eqs. (7) and (8) because inclusion of these terms does not significantly alter the behavior of $\nu'_{xr}/\nu'_{r\theta}$ and $\nu''_{xr}/\nu''_{r\theta}$ seen in Fig. 13. This same conclusion (no improvement) applies even if the overall algebraic Reynolds stress model is modified to include convection and diffusion effects, e.g., by means of the model proposed by Rodi.[21] Thus, algebraic modeling of the individual Reynolds stress components is basically inadequate for the present flow situation. A similar conclusion was reached by Franke et al.,[22] who examined the applicability of conventional eddy viscosity and algebraic Reynolds stress models to flow about a circular cylinder with vortex shedding.

Transport equation models of swirling turbulent flows sometimes include a Richardson number correction in their formulation, often in the form of an ad hoc modification to the dissipation rate equation. It is generally acknowledged that a gradient-type Richardson number performs well for predicting flow over spinning surfaces, whereas a flux-type Richardson number is more appropriate for weakly swirling jet flows.[17,23,24] For strongly swirling jet flows, Leschziner and Rodi[25] have shown that the standard form of the k-ϵ model performs better if no Richardson number correction is included in the model, provided that realistic initial conditions are specified for the computations. Further refinements in the standard k-ϵ model are still needed, however, if strongly swirling jet flows are to be predicted with reasonable accuracy.[26] Recent work in this area has led to the development of an improved pressure-strain model for swirling jet flows with recirculation,[27] and demonstrated the need for closure at the full Reynolds stress transport equation level in order to predict both weakly and strongly swirling jet flows with higher accuracy.[28]

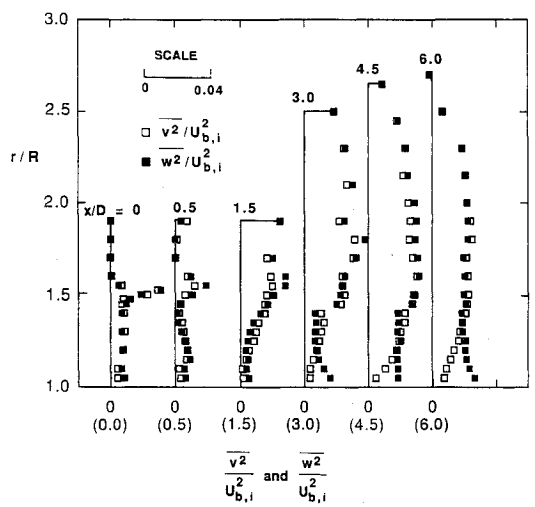

Fig. 12 Turbulent normal stress profiles.

Inasmuch as the present flow is a moderately swirling flow, examination of Richardson number behavior is of interest. For this purpose, gradient-and flux-type Richardson numbers were evaluated from the data utilizing expressions prescribed by Rodi,[24] namely,

$$Ri_f = \frac{2\,\overline{vw}\,(W/r)}{-\overline{uv}(\partial U/\partial r) - \overline{vw}\,r\partial(W/r)/\partial r} \tag{13}$$

$$Ri_g = \frac{2(W/r^2)\partial(rW)/\partial r}{(\partial U/\partial r)^2 + [r\partial(W/r)/\partial r]^2} \tag{14}$$

These Richardson numbers can be compared with the radial rate of change of tangential angular momentum in the flow, namely,

$$M = \frac{1}{r}\frac{\partial(rW)}{\partial r} \tag{15}$$

If M is positive, then the presence of swirl will have a stabilizing (turbulence suppressing) effect on the flow, whereas a negative value of M will have a destabilizing influence and lead to turbulence amplification. If a particular Richardson number is performing properly, then the sign of Ri should correlate with the sign of M in order to model the stabilizing or destabilizing influence of swirl on the flow.

Figure 14 shows distributions of M, Ri_f, and Ri_g, as evaluated along radial traverses at three axial stations ($x/D = 0.5$,

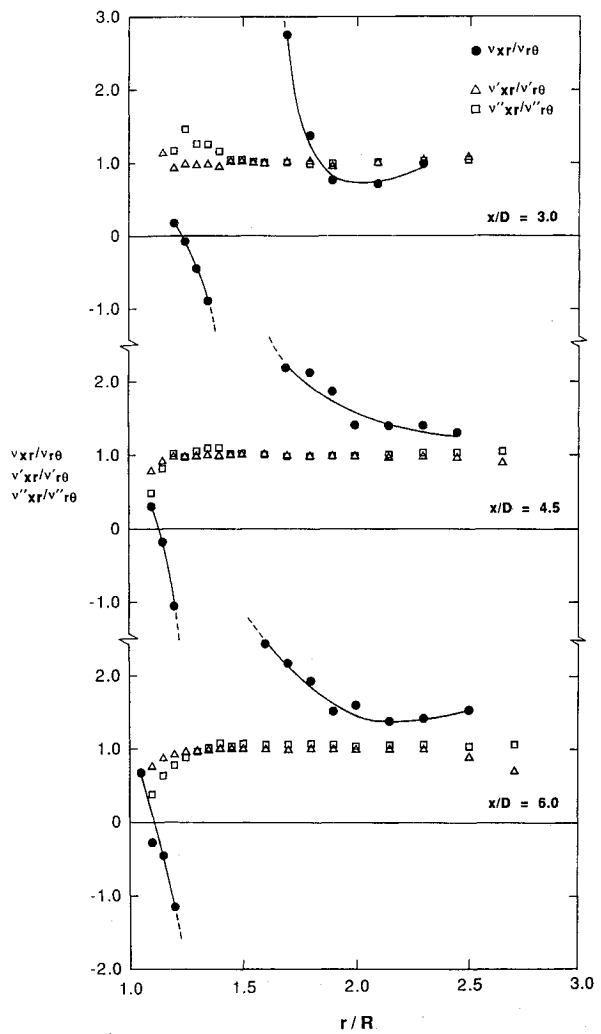

Fig. 13 Eddy viscosity ratio distributions.

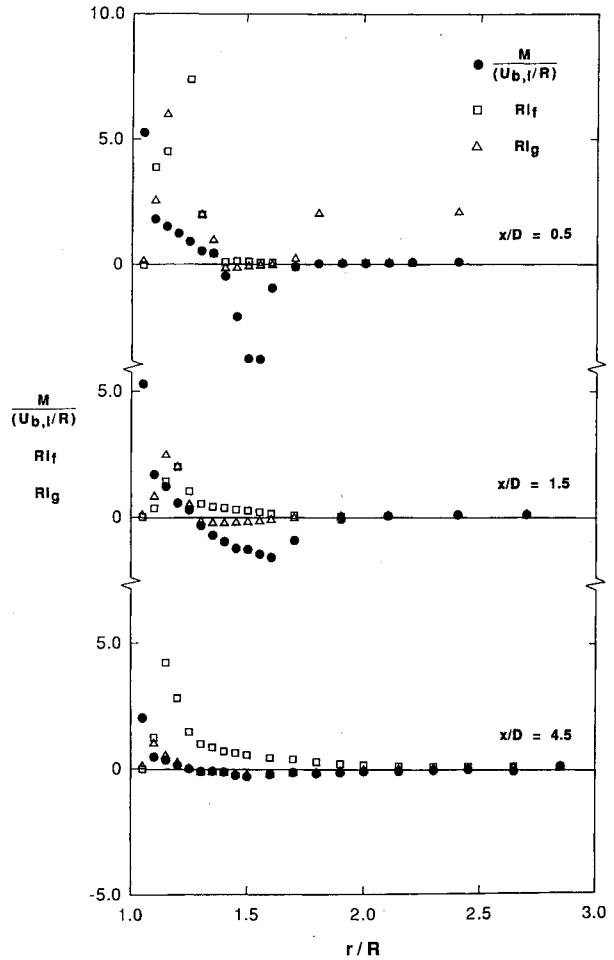

Fig. 14 Radial gradient of tangential angular momentum and Richardson number distributions.

1.5, and 4.5). In reference to the results shown at $x/D = 0.5$, it can be seen that negative values of M exist near $r/R = 1.5$, which is just downstream of the nozzle lip that separates the inner and outer streams. Swirl in this region has a destabilizing influence on the flow, therefore, which diminishes in the downstream direction, as indicated by the results shown at $x/D = 1.5$ and 4.5. Although the gradient Richardson number simulates this behavior, the flux Richardson number does not, because it remains positive across the width of the shear layer. Figure 14 also shows that neither the gradient nor the flux Richardson number simulates the stabilizing influence of swirl near the centerbody surface, where M is positive and decays with increasing radius, but Ri_f and Ri_g are both close to zero. This behavior is directly attributable to vortex-induced effects in the flow on the basis of the following considerations. Figure 7b shows that $\overline{vw}$ is near zero in the immediate vicinity of the centerbody surface, whereas the mean strain rate $r\,\partial(W/r)/\partial r$ in this region (indicated by the dashed-line distributions) is definitely not zero. As noted earlier, this behavior represents a departure from local equilibrium induced by coherent vortical structures near the centerbody surface. In reference to Eq. (13), near-zero values of $\overline{vw}$ in the vicinity of the centerbody surface are responsible for Ri_f being close to zero at $r/R = 1.05$, as shown in Fig. 14. In reference to Eq. (14) and Fig. 7, the relatively high mean strain rates at $r/R = 1.05$ account for Ri_f being close to zero at a point where M is strongly positive. The need to model the behavior of M via a gradient- or flux-type Richardson number may not be an issue, however, inasmuch as recent work has shown that full Reynolds stress transport equation models applied to swirling turbulent jet flows perform well without a Richardson number correction.[27,28]

Concluding Remarks

The turbulent mixing of two coannular streams with swirl present in the inner stream has been investigated experimentally. The inner stream was bounded by a centerbody, but the outer stream was unconfined and exposed to the atmosphere. The results show that the flow is dominated by the presence of vortices that are shedding periodically from the lips of the nozzle. These vortices provide a mechanism for amplifying Reynolds stress levels in the flow without simultaneously inducing an increase in mean strain rates. The presence of coherent vortical structures causes the mean swirl angle to oscillate, especially in the low-momentum region adjacent to the centerbody surface. Turbulent mixing is enhanced to the extent that mean strain rates in the inner region are reduced as the flow proceeds downstream, whereas turbulence intensity levels simultaneously increase as a result of vortex passage or vortex breakup when the inner shear layer interacts with the center boundary layer.

The coherent vortical structures also cause large departures from local equilibrium, so that significant phase differences exist between resultant shear stress and mean strain rate angles in the flow. This behavior is reflected in eddy viscosity component values that differ significantly throughout the flow and, at times, are negative. Analysis of the results shows that turbulence kinetic energy levels increase in regions of the flow where the turbulence kinetic energy production rate is decreasing. This behavior can be attributed to vortex-induced turbulence amplification effects in the flow. The results also indicate that conventionally defined gradient and flux-type Richardson numbers do not simulate observed rates of change of tangential angular momentum across the shear layer.

On the basis of these observations, it can be concluded that neither conventional eddy viscosity modeling nor k-ϵ type modeling with an algebraic stress model is adequate for predicting the present flow situation. Closure at the full Reynolds stress transport equation level also has its limitations because of the difficulties associated with modeling time-dependent (vortex shedding) phenomena by means of statistically based turbulence models. Direct numerical simulation of the unsteady form of the Navier-Stokes equation offers the most promising alternative, but present methods are currently unable to resolve the small-scale motion in high Reynolds number flows. In spite of these modeling and simulation difficulties, the data that have been obtained constitute an interesting test case for comparison with numerical predictions. Tabulated data are available for this purpose in a thesis that forms the basis of the present paper.[29]

Acknowledgment

The authors would like to express their appreciation to the Air Force Office of Scientific Research who sponsored this work under AFOSR Grant 85-0273.

References

[1]Champagne, F. H., and Wygnanski, I. J., "An Experimental Investigation of Coaxial Turbulent Jets," *International Journal of Heat and Mass Transfer*, Vol. 14, No. 9, 1971, pp. 1445-1464.

[2]Durão, D. and Whitelaw, J. H., "Turbulent Mixing in the Developing Region of Coaxial Jets," *Journals of Fluids Engineering*, Transactions ASME, Vol. 95, Sept. 1973, pp. 467-473.

[3]Ribeiro, M. M., and Whitelaw, J. H., "Turbulent Mixing of Coaxial Jets with Particular Reference to the Near-Exit Region," *Journal of Fluids Engineering*, Transactions ASME, Vol. 98, June 1976, pp. 284-291.

[4]Ribeiro, M. M., and Whitelaw, J. H., "Coaxial Jets With and Without Swirl," *Journal of Fluid Mechanics*, Vol. 96, Part 4, 1980, pp. 769-795.

[5]Lau, J. C., and Fisher, M. J., "The Vortex-Street Structure of Turbulent Jets, Part 1," *Journal of Fluid Mechanics*, Vol. 67, Part 2, 1975, pp. 299-337.

[6]Bruun, H. H., "A Time-Domain Analysis of the Large-Scale Flow

Structure in a Turbulent Jet, Part 1, Moderate Reynolds Number," *Journal of Fluid Mechanics*, Vol. 83, Part 4, 1977, pp. 641-671.

[7]Ko, N. W. M., and Kwan, A. S. H., "The Initial Region of Subsonic Coaxial Jets," *Journal of Fluid Mechanics*, Vol. 73, Part 2, 1976, pp. 305-332.

[8]Kwan, A. S. H., and Ko, N. W. M., "The Initial Region of Subsonic Coaxial Jets, Part 2," *Journal of Fluid Mechanics*, Vol. 82, Part 2, 1977, pp. 273-287.

[9]Ko, N. W. M., and Lam, K. M., "Flow Structures of Coaxial Jet of Mean Velocity Ratio 0.5," *AIAA Journal*, Vol. 27, No. 5, 1989, pp. 513-514.

[10]Lau, J. C., Fisher, M. J., and Fuchs, H. V., "The Intrinsic Structure of Turbulent Jets," *Journal of Sound and Vibration*, Vol. 22, No. 4, 1972, pp. 379-406.

[11]Frey, M. O., and Gessner, F. B., "Mean Flow Field and Reynolds Stress Behavior in Coannular Jet Flow with Swirl Along a Centerbody," *Benchmark Test Cases for Computational Fluid Dynamics*, FED-Vol. 93, American Society of Mechanical Engineers, 1990, pp. 29-37; also, *Journal of Fluids Engineering* (to be published).

[12]Mattingly, J. D., and Oates, G. C., "An Experimental Investigation of the Mixing of Coannular Swirling Flows," *AIAA Journal*, Vol. 24, No. 5, 1986, pp. 785-792.

[13]Al-Beirutty, M. H., and Gessner, F. B., "A Hot-Wire Measurement Technique for Moderate Intensity, Skewed Turbulent Flows," *Proceedings of the Seventh Symposium on Turbulent Shear Flows*, Vol. 2, Stanford Univ., Stanford, CA, 1989, pp. 19.3.1-19.3.6.

[14]Al-Beirutty, M. H., "Development of a Hot-Wire Measurement Technique for Moderate Intensity, Three-Dimensional Flow," Ph.D. Thesis, Dept. of Mechanical Engineering, Univ. of Washington, Seattle, WA, 1987.

[15]Fernholz, H. H., and Vagt, J. -D., "Turbulence Measurements in an Adverse-Pressure-Gradient Three-Dimensional Turbulent Boundary Layer Along a Circular Cylinder," *Journal of Fluid Mechanics*, Vol. 111, Oct. 1981, pp. 233-269.

[16]Driver, D. M., and Hebbar, S. K., "Experimental Study of a Three-Dimensional, Shear-Driven, Turbulent Boundary Layer," *AIAA Journal*, Vol. 25, No. 1, 1987, pp. 35-42.

[17]Morse, A. P., "Axisymmetric Free Shear Flows With and Without Swirl," Ph.D. Thesis, Mechanical Engineering Dept., Imperial College of Science and Technology, London, May 1980.

[18]Higuchi, H., and Rubesin, M. W., "Behavior of a Turbulent Boundary Layer Subjected to Sudden Transverse Strain," *AIAA Journal*, Vol. 17, No. 9, 1979, pp. 931-941.

[19]Launder, B. E., Reece, G. J., and Rodi, W., "Progress in the Development of a Reynolds-Stress Turbulence Closure," *Journal of Fluid Mechanics*, Vol. 68, Part 3, 1975, pp. 537-566.

[20]Naot, D., Shavit, A., and Wolfstein, M., "Interaction Between Components of the Turbulent Velocity Correlation Tensor Due to Pressure Fluctuations," *Israel Journal of Technology*, Vol. 8, No. 3, 1970, pp. 259-269.

[21]Rodi, W., "A New Algebraic Relation for Calculating the Reynolds Stresses," *ZAMM*, Vol. 56, No. 3, 1976, pp. T219-T221.

[22]Franke, R., Rodi, W., and Schönung, B., "Analysis of Experimental Vortex-Shedding Data with Respect to Turbulence Modeling," *Proceedings of the Seventh Symposium on Turbulent Shear Flows*, Vol. 2, Stanford Univ., Stanford, CA, 1989, pp. 24.4.1 -24.4.6.

[23]Bradshaw, P., "Effects of Streamline Curvature on Turbulent Flow," AGARDograph 169, 1973.

[24]Rodi, W., "Influence of Buoyancy and Rotation on Equations for the Turbulent Length Scale," *Proceedings of the Second Symposium on Turbulent Shear Flows*, Imperial College, London, July 1979, pp. 10.37-10.42.

[25]Leschziner, M. A., and Rodi, W., "Computation of Strongly Swirling Axisymmetric Free Jets," *AIAA Journal*, Vol. 22, No. 12, 1984, pp. 1742-1747.

[26]Truelove, J. S., and Mahmud, T., "Calculation of Strongly Swirling Jet Flows," *Proceedings of the Ninth Australasian Fluid Mechanics Conference*, Univ. of Auckland, New Zealand, Dec. 1988, pp. 492-495.

[27]Fu, S., Launder, B. E., and Leschziner, M. A., "Modeling Strongly Swirling Recirculating Jet Flow with Reynolds-Stress Transport Closures," *Proceedings of the Sixth Symposium on Turbulent Shear Flows*, Paul Sabatier Univ., Toulouse, France, Sept. 1987, pp. 17.61-17.6.6.

[28]Fu, S., Huang, P. G., Luander, B. E., and Leschziner, M. A., "A Comparison of Algebraic and Differential Second-Moment Closures for Axisymmetric Turbulent Shear Flows With and Without Swirl," *Journal of Fluids Engineering*, Vol. 110, June 1988, pp. 216-221.

[29]Frey, M. O., "Investigation of an Unconfined Coannular Jet Flow with Swirl Along a Centerbody," M.S. Thesis, Dept. of Aeronautics and Astronautics, Univ. of Washington, Seattle, WA, 1990.